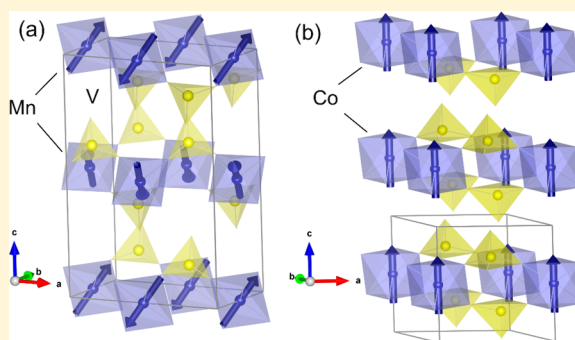


Magnetic Ground State Crossover in a Series of Glaserite Systems with Triangular Magnetic Lattices

Liurukara D. Sanjeewa,^{†,§} V. Ovidiu Garlea,[‡] Michael A. McGuire,[§] Colin D. McMillen,[†] and Joseph W. Kolis^{*,†}[†]Department of Chemistry and Center for Optical Materials Science and Engineering Technologies (COMSET), Clemson University, Clemson, South Carolina 29634-0973, United States[‡]Neutron Scattering Division and [§]Materials Science and Technology Division, Oak Ridge National Laboratory, Oak Ridge, Tennessee 37831, United States

Supporting Information

ABSTRACT: The magnetic properties are reported for three members of the glaserite series of compounds, $\text{Na}_2\text{BaM}(\text{VO}_4)_2$, $\text{M} = \text{Mn}$, $\text{Mn}_{0.6}\text{Co}_{0.4}$, and Co . Large single crystals are grown using a high-temperature hydrothermal synthesis method. This structure type exhibits a triangular magnetic lattice in which M^{2+}O_6 octahedra are interconnected with nonmagnetic $(\text{VO}_4)^{3-}$ groups. All the structures crystallize at room temperature with rigid trigonal symmetry (space group $P\bar{3}m1$); however, at lower temperatures both $\text{Na}_2\text{BaMn}(\text{VO}_4)_2$ and $\text{Na}_2\text{BaMn}_{0.6}\text{Co}_{0.4}(\text{VO}_4)_2$ undergo a structural transition to lower symmetry (monoclinic, $C2/c$). The bulk magnetic measurements indicate that Mn- and Co-structures are antiferromagnetic and ferromagnetic, respectively. $\text{Na}_2\text{BaMn}_{0.6}\text{Co}_{0.4}(\text{VO}_4)_2$ does not show any long-range ordering down to 0.5 K, although a broad heat capacity anomaly near 1.2 K suggests short-range magnetic order or freezing into a spin-glass-like state related to the chemical disorder and resulting competing magnetic interactions. The magnetic structures of $\text{Na}_2\text{BaMn}(\text{VO}_4)_2$ and $\text{Na}_2\text{BaCo}(\text{VO}_4)_2$ were determined using neutron powder diffraction. At zero magnetic field, $\text{Na}_2\text{BaMn}(\text{VO}_4)_2$ possesses an antiferromagnetic structure with the moments ordered in a Néel-type arrangement and aligned along the C_4 axis of the octahedra. Under applied magnetic field at 0.3 K, the evolution of the magnetic structure toward a fully polarized state is observed. $\text{Na}_2\text{BaCo}(\text{VO}_4)_2$ represents a ferromagnetic (FM) magnetic structure with Co moments aligned parallel to the c -axis direction. The relationships between these structures and magnetic properties are discussed.



1. INTRODUCTION

Structures containing two-dimensional (2D) magnetic lattices are of considerable interest due to potential geometrical frustration and spin fluctuation which can lead to a variety of exotic magnetic behaviors at low temperatures including quantum spin liquids and spin ices.^{1–7} Triangular lattices (TL) are considered to be the simplest model of a geometrically frustrated magnetic framework, with isolated magnetic ions forming equilateral triangles via linkages with nonmagnetic bridging groups like halides or oxyanions. This class of compounds has received special attention recently.^{8–10} The magnetic spins of the triangular lattice (TL) could order antiferromagnetically (TLA) to each other at zero magnetic field where spins are 120° relative to one another within the triangle. In an applied magnetic field, this magnetic structure can transform into the so-called Y-phase, in an up–up–down (*uud*) fashion or into a 2:1 canted magnetic structure.^{11–16}

The magnetic ground state of the triangular lattice is typically sensitive to the symmetry of the transition metal–nonmagnetic layer since the magnetic superexchange happens through these nonmagnetic oxyanion groups. Therefore,

preservation of 3-fold crystallographic symmetry in the parent compound is a critical factor in the formation of a geometrically frustrated lattice.^{11,17–21} In some cases, however, a structural transition can be observed at lower temperatures, and this can reduce the geometric frustration by removing the rigid 3-fold symmetry in the lattice. For example, $\text{KFe}(\text{MoO}_4)_4$ undergoes a phase transition to a monoclinic structure at low temperatures, which results two independent magnetic subsystems and leads to a complex three-dimensional or unconventional quasi-two-dimensional magnetic ordering.^{22,23} So far, a limited number of high symmetry TL magnetic structures have been reported, and furthermore, growth of these as large high quality single crystals has been very limited. It is a daunting challenge to synthetic chemists to identify novel materials with perfect triangular magnetic lattices and to subsequently grow sufficiently large single crystals to enable detailed measurements and perform structure–property correlations.

Received: December 12, 2018

Published: February 7, 2019

Among the most recently studied TL systems, $\text{RbFe}(\text{MoO}_4)_2$ ¹¹ and $\text{A}_3\text{M}'\text{M}''_2\text{O}_9$ with $\text{A} = \text{Ba}$ or Sr , $\text{M}' = \text{Ni}$, Co , Mn , and $\text{M}'' = \text{Nb}$, Sb , or Ta ^{17–20} have attracted interest due to their multiferroic properties. In contrast to the other oxyanions (XO_6 or XO_4 , $\text{X} = \text{P}$, Mo , Nb^{5+} , Ta^{5+} , and Sb^{5+}), detailed structure–property correlations of higher symmetry, transition metal vanadates with trigonal lattices are somewhat scarce. Among these, $\text{BaAg}_2\text{M}(\text{VO}_4)_2$ ($\text{M} = \text{Co}$, Ni) and $\text{AAg}_2\text{Fe}(\text{VO}_4)_2$ ($\text{A} = \text{K}$ and Rb) are high-symmetry transition metal vanadate compound series with trigonal lattices.^{24,25} The $\text{BaAg}_2\text{M}(\text{VO}_4)_2$ series belongs to a rare class of ferromagnetic insulators, while the $\text{AAg}_2\text{Fe}(\text{VO}_4)_2$ system possesses TLA with XY-anisotropy. Considering the significance of the few known cases, it is important to investigate any new TL transition metal vanadates in detail to compare the similarities and differences with other reported high-symmetry trigonal transition metal solids.

Previously, we reported the high-temperature high-pressure hydrothermal synthesis and structure of series of the glaserite type $\text{A}_2\text{AEM}(\text{VO}_4)_2$ ($\text{A} = \text{Li}$, Na , K ; $\text{AE} = \text{Sr}$, Ba ; and $\text{M} = \text{Mn}$, Fe , Co) structures.^{26,27} This family of compounds crystallizes in various space groups depending upon the alkali and alkaline earth metal cation in the structure. For example, the series $\text{A}_2\text{BaM}(\text{VO}_4)_2$ ($\text{A} = \text{K}$, Na , $\text{M} = \text{Mn}$, Fe , Co) crystallizes in $\text{P}\bar{3}m1$, $\text{Li}_2\text{BaMn}(\text{VO}_4)_2$ in $\text{P}\bar{3}$, and $\text{Na}_2\text{SrM}(\text{VO}_4)_2$ ($\text{M} = \text{Mn}$, Co) in lower symmetry monoclinic $\text{P}2_1/c$.²⁶ As a common feature, these compounds consist of 2D transition metal vanadate layers ($\text{M}-\text{O}-\text{V}$) built from corner sharing M^{2+}O_6 octahedra ($\text{M} = \text{Mn}$, Fe , Co), and VO_4 tetrahedra, while the alkali and alkaline earth metal cations reside between the layers.²⁶ Since the transition metal octahedra are well isolated from one another, any magnetic exchange occurs via superexchange through the nonmagnetic VO_4 groups. Hence, the relative orientation between M^{2+}O_6 -octahedra and VO_4 -tetrahedra within the 2D layer is very important to describe the magnetic properties in these glaserite-type compounds. Moreover, this structural feature can be fine-tuned using different counterions between the 2D layers, which eventually results different space groups in the general class of glaserite-type compounds.²⁶

As the first step of investigating all the intriguing ground states, we studied the magnetic structure of Fe^{2+} -glaserite compound, $\text{Na}_2\text{BaFe}(\text{VO}_4)_2$, and observed a structural phase transition at ~ 290 K to a low temperature monoclinic structure. The magnetization measurements along with single crystal neutron diffraction studies showed that it orders into a canted ferromagnetic structure below 7 K.²⁷ On the other hand, the magnetic properties of triangular magnetic lattices compound series of $\text{Na}_2\text{BaM}(\text{VO}_4)_2$, with $\text{M} = \text{Mn}$, Co , Ni have been reported by Nakayama et al.²⁸ This series of compounds share very similar structural features with $\text{Na}_2\text{BaM}(\text{VO}_4)_2$ $\text{M} = \text{Mn}$, Fe , Co series which was reported in ref 26 previously from our research group, along with a detailed crystallographic comparison. According to Nakayama et al., the magnetization data indicated that $\text{Na}_2\text{BaMnV}_2\text{O}_8$ is antiferromagnetic, while both $\text{Na}_2\text{BaCoV}_2\text{O}_8$ and $\text{Na}_2\text{BaNiV}_2\text{O}_8$ are ferromagnetic. This variation in magnetic behavior has motivated us to undertake a comprehensive study on these $\text{Na}_2\text{BaM}(\text{VO}_4)_2$ polymorphs to gain a deeper understanding of the correlation between structural and magnetic properties and to establish their magnetic structures.

Here we report the crystallographic structural transitions, magnetic properties and magnetic structures of Na_2BaM -

$(\text{VO}_4)_2$ glaserites where $\text{M} = \text{Mn}^{2+}$, Co^{2+} and a mixed composition of $\text{Mn}_{0.4}\text{Co}_{0.6}$. All compounds crystallize in trigonal crystal system with space group of $\text{P}\bar{3}m1$ at room temperature where $a \sim 5.7$ Å and $c \sim 7.3$ Å. Like the previously reported Fe-based compound, $\text{Na}_2\text{BaMn}(\text{VO}_4)_2$ and $\text{Na}_2\text{Ba}(\text{Mn},\text{Co})(\text{VO}_4)_2$ undergo a structural transition at lower temperature from the trigonal $\text{P}\bar{3}m1$ to monoclinic $\text{C}2/c$. Interestingly, the $\text{Na}_2\text{BaCo}(\text{VO}_4)_2$ does not undergo any structural transition. Regardless of the subtle crystallographic differences, the magnetic properties of $\text{Na}_2\text{BaMn}(\text{VO}_4)_2$ and $\text{Na}_2\text{BaCo}(\text{VO}_4)_2$ are consistent with previous findings²⁸ where the Mn-glaserite exhibits an antiferromagnetic ordered state while the Co compound orders ferromagnetically. We find that the intermediate member of the series, $\text{Na}_2\text{BaMn}_{0.4}\text{Co}_{0.6}(\text{VO}_4)_2$, exhibits no long-range magnetic order down to 2 K, with a broad heat capacity anomaly centered near 1.2 K, likely related to short-range magnetic correlations or spin glass-like state arising from competing magnetic interactions.

2. EXPERIMENTAL SECTION

A high-temperature, high-pressure hydrothermal technique was employed to synthesize the single crystals of $\text{Na}_2\text{BaMn}(\text{VO}_4)_2$, $\text{Na}_2\text{BaCo}(\text{VO}_4)_2$ and $\text{Na}_2\text{BaMn}_{0.4}\text{Co}_{0.6}(\text{VO}_4)_2$. All the reactions were performed in 2.5 in. long silver ampules with a diameter of 3/8 in. To synthesize single crystals of $\text{Na}_2\text{BaMn}(\text{VO}_4)_2$, a mixture of Na_2CO_3 (Aldrich, 99%), BaO (Alfa Aesar, 99.5%), Mn_2O_3 (Alfa Aesar, 99.99%), and V_2O_5 (Alfa Aesar, 99.6%) were mixed in a molar ratio of 2:2:1:2. A total of 0.4 g of reactants (Na_2CO_3 (0.0815 g); BaO (0.1179 g); Mn_2O_3 (0.0607 g); V_2O_5 (0.1399 g)) were mixed with 0.8 mL of 5 M NaOH in silver ampules. For $\text{Na}_2\text{BaCo}(\text{VO}_4)_2$, a mixture of Na_2CO_3 , BaO , Co_3O_4 (Alfa Aesar, 99.99%), and V_2O_5 mixed in a stoichiometric ratio of 2:2:1:2. Similarly, 0.4 g of a mixture of Na_2CO_3 (0.0755 g), BaO (0.1092 g), Co_3O_4 (0.0858 g), and V_2O_5 (0.1295 g) was used with 0.8 mL of 5 M NaOH. After loading the reactants and the mineralizer, the silver ampules were weld-sealed and heated in a Tuttle-sealed autoclave filled with water to provide suitable counter pressure at 580 °C for 2 weeks. After the reaction time, yellow crystals of $\text{Na}_2\text{BaMn}(\text{VO}_4)_2$ (size ~ 2 mm, 80% yield) and dark blue single crystals of $\text{Na}_2\text{BaCo}(\text{VO}_4)_2$ (size ~ 2 mm, 80% yield) were isolated using suction filtration.

A different approach was used to synthesize the mixed Mn and Co glaserite phase. First, a polycrystalline sample with a target composition of $\text{Na}_2\text{BaMn}_{0.5}\text{Co}_{0.5}(\text{VO}_4)_2$ was synthesized. Herein, a total of 2 g of reactants of Na_2CO_3 (0.4123 g), BaO (0.5965 g), MnO (Alfa Aesar, 99%, 0.1380 g), CoO (Alfa Aesar, 99%, 0.1457 g), and V_2O_5 (0.7075 g) were used in a molar ratio of 2:2:1:1:2. All the reactants were mixed and ground thoroughly using an agate mortar and pestle. After that, the mixture was preheated to 300 °C for 6 h. Then, the mixture was reground, pressed, and calcined for 2 days at 800 °C under Ar flow in a tube furnace. The powder X-ray diffraction pattern is given in the Figure SI 1. In order to grow single crystals, 0.4 g of the resulting powder was mixed with 0.8 mL of 5 M NaOH in 2.5 in. long, 3/8 in. diameter silver ampules. Finally, reactions were loaded into the Tuttle-sealed autoclave and filled with water to provide counterpressure. Reactions were performed at 580 °C for 2 weeks. After the reactions, red crystals were isolated at a lower yield with rest of the unreacted powder. Single crystal growth of other mixed Mn/Co derivatives has been unsuccessful so far.

The powder samples of $\text{Na}_2\text{BaMn}(\text{VO}_4)_2$ and $\text{Na}_2\text{BaCo}(\text{VO}_4)_2$ used for the neutron powder diffraction experiments were synthesized using a conventional solid state method. Herein, a mixture of 5 g of Na_2CO_3 (1.0348 g), BaO (1.4970 g), MnO (0.6926 g) and V_2O_5 (1.7757 g) was used in the stoichiometric ratio of 1:1:1:1. A similar stoichiometric ratio was also used in the case of $\text{Na}_2\text{BaCo}(\text{VO}_4)_2$ (Na_2CO_3 (1.0268 g), BaO (1.4854 g), CoO (0.7259 g) and V_2O_5 (1.7620 g)). All the reactions were mixed, ground and heated to 300

Table 1. Crystallographic Data of Na₂BaMn(VO₄)₂, Na₂BaMn_{0.6}Co_{0.4}(VO₄)₂, and Na₂BaCo(VO₄)₂ at Room Temperature

empirical formula	Na ₂ BaMn(VO ₄) ₂	Na ₂ BaMn _{0.4} Co _{0.6} (VO ₄) ₂	Na ₂ BaCo(VO ₄) ₂
FW	468.14	469.74	472.13
crystal system	trigonal	trigonal	trigonal
crystal dimensions, mm	0.10 × 0.08 × 0.04	0.08 × 0.08 × 0.06	0.12 × 0.10 × 0.04
space group, Z	$P\bar{3}m1$ (No. 164), 1	$P\bar{3}m1$ (No. 164), 1	$P\bar{3}m1$ (No. 164), 1
T, K	298	298	298
a, Å	5.5929(2)	5.5761(2)	5.5440(2)
c, Å	7.1540(4)	7.1245(5)	7.0668(4)
V, Å ³	193.800(18)	191.843(19)	188.105(17)
D (calcd, g/cm ³)	4.011	4.066	4.168
F(000)	213	214	215
μ (Mo Kα), mm ⁻¹	9.062	9.361	9.863
T _{max} T _{min}	1.000, 0.8691	1.000, 0.5986	1.000, 0.8210
2θ range	2.85–26.30	2.86–26.40	2.88–26.37
no. of reflections	4031	4533	3651
data/restraints/parameters	178/6/21	178/6/21	172/0/21
final R [I > 2σ(I)] R ₁ , wR ₂	0.0373/0.0802	0.0317/0.0705	0.0282/0.0579
final R (all data) R ₁ , wR ₂	0.0415/0.0984	0.0318/0.0705	0.0282/0.0579
GOF	1.102	1.159	1.129
largest diff. peak/hole, e/Å ³	1.781/–1.516	1.364/–1.262	1.030/–1.423

Table 2. Crystallographic Data of Na₂BaMn(VO₄)₂, Na₂BaMn_{0.6}Co_{0.4}(VO₄)₂, and Na₂BaCo(VO₄)₂ at Lower Temperatures

empirical formula	Na ₂ BaMn(VO ₄) ₂	Na ₂ BaMn _{0.6} Co _{0.4} (VO ₄) ₂	Na ₂ BaCo(VO ₄) ₂
FW	468.14	469.74	472.13
crystal system	monoclinic	monoclinic	trigonal
crystal dimensions, mm	0.10 × 0.08 × 0.04	0.08 × 0.08 × 0.06	0.12 × 0.10 × 0.04
space group, Z	C2/c (No. 15), 4	C2/c (No. 15), 4	$P\bar{3}m1$ (No. 164), 1
T, K	123	153	150
a, Å	9.5922(6)	9.6008(9)	5.5360(5)
b, Å	5.6275(4)	5.5628(5)	
c, Å	14.2358(11)	14.1508(13)	7.0611(7)
β, (deg)	90.184(3)	90.086(4)	
V, Å ³	768.45(9)	755.76(12)	187.41(4)
D (calcd, g/cm ³)	4.046	4.128	4.183
μ (Mo Kα), mm ⁻¹	9.142	9.505	9.899
F(000)	852	855	215
T _{max} T _{min}	1.000, 0.8516	1.0000, 0.3302	1.000, 0.8375
2θ range	2.86–26.00	2.88–25.48	2.88–25.85
no. of reflections	3296	3451	1950
data/restraints/parameters	746/0/67	778/0/68	163/6/21
final R [I > 2σ(I)] R ₁ , wR ₂	0.0554/0.1441	0.0837/0.1869	0.0343/0.0845
final R (all data) R ₁ , wR ₂	0.0561/0.1444	0.0856/0.1881	0.0347/0.0851
GOF	1.207	1.164	1.149
largest diff. peak/hole, e/Å ³	4.094/–5.504	4.723/–3.857	1.458/–1.386

°C for 6 h as the first step. After that, the resultant powders were pressed into pellets and calcined at 800 °C for 2 days. As a final step, several reheating and regrinding iterations were performed until no further impurities present in the sample. The room-temperature PXRD was performed using a Rigaku Ultima IV diffractometer with Cu Kα radiation ($\lambda = 1.5406$ Å) at 0.02° intervals at a rate of 0.1°/min from 5 to 65°. Additionally, temperature-dependent powder X-ray diffraction data was collected on ground single crystals of Na₂BaMn_{0.6}Co_{0.4}(VO₄)₂ using a PANalytical X'Pert Pro MPD with an Oxford PheniX cryostat. The PXRD patterns are given in Figures SI 1–2.

Single crystal X-ray diffraction was performed in a temperature range from 300 to 125 K to investigate the structural evolution of Na₂BaMn(VO₄)₂, Na₂BaMn_{0.6}Co_{0.4}(VO₄)₂ and Na₂BaCo(VO₄)₂. X-ray data was collected using a Bruker D8 Venture instrument equipped with an Incoatec Mo Kα microfocus source ($\lambda = 0.71073$ Å) and Photon 100 CMOS detector. The structures were solved by intrinsic phasing and refined by full-matrix least-squares techniques on

F^2 using the SHELXTL software package.²⁹ Unit cell parameters and selected interatomic distances and angles are summarized in Tables 1–3, and positional parameters are given in the Tables SI 1–3. Energy-dispersive spectroscopy analysis (EDS) was performed using a Hitachi S-3400 scanning electron microscope equipped with an OXFORD EDX microprobe to identify the elemental composition in both single crystals and the powder samples (Table SI 4).

Magnetization measurements were performed using a Quantum Design Magnetic Property Measurement System (SQUID magnetometer). Single crystals (2–3 mg each) were affixed to a fused silica rod using GE varnish and placed inside plastic drinking straws for the measurements. Heat capacity measurements were performed on single crystals (2–5 mg each) using a Quantum Design Physical Property Measurement System with the Helium-3 option.

Neutron powder diffraction measurements were performed on the glaserite samples with M = Mn and Co, using the HB2A Powder Diffractometer at High Flux Isotope Reactor (HFIR) at Oak Ridge National Laboratory. Diffraction patterns were collected using the

Table 3. Selected Interatomic Distances (Å) and Angles (deg) of Na₂BaMn(VO₄)₂, Na₂BaCo(VO₄)₂, and Na₂BaMn_{0.6}Co_{0.4}(VO₄)₂ at Room Temperature and Lower Temperatures

$\bar{P}3m1$ - Na ₂ BaMn(VO ₄) ₂		$\bar{P}3m1$ - Na ₂ BaMn _{0.6} Co _{0.4} (VO ₄) ₂		$\bar{P}3m1$ - Na ₂ BaCo(VO ₄) ₂	
Mn(1)–O(2) × 6	2.118(11)	Mn/Co(1)–O(2) × 6	2.099(7)	Co(1)–O(2) × 6	2.065(6)
V(1)–O(1)	1.681(14)	V(1)–O(1)	1.680(10)	V(1)–O(1)	1.679(8)
V(1)–O(2) × 3	1.681(11)	V(1)–O(2) × 3	1.685(7)	V(1)–O(2) × 3	1.685(7)
Mn(1)–O(2)–V(1)	161.8(6)	Mn/Co(1)–O(2)–V(1)	161.6(4)	Co(1)–O(2)–V(1)	162.3(4)
C2/c - Na ₂ BaMn(VO ₄) ₂		C2/c - Na ₂ BaMn _{0.6} Co _{0.4} (VO ₄) ₂		C2/c - Na ₂ BaCo(VO ₄) ₂	
Mn(1)–O(2) × 2	2.176(10)	Mn/Co(1)–O(2) × 2	2.15(2)		
Mn(1)–O(3) × 2	2.134(10)	Mn/Co(1)–O(3) × 2	2.08(2)		
Mn(1)–O(4) × 2	2.158(10)	Mn/Co(1)–O(4) × 2	2.12(2)		
V(1)–O(1)	1.683(10)	V(1)–O(1)	1.691(16)		
V(1)–O(2)	1.717(11)	V(1)–O(2)	1.69(2)		
V(1)–O(3)	1.732(10)	V(1)–O(3)	1.73(2)		
V(1)–O(4)	1.711(10)	V(1)–O(4)	1.70(2)		
Mn(1)–O(2)–V(1)	162.5(6)	Mn/Co(1)–O(2)–V(1)	165.3(17)		
Mn(1)–O(3)–V(1)	142.1(6)	Mn/Co(1)–O(3)–V(1)	145.3(11)		
Mn(1)–O(4)–V(1)	146.7(6)	Mn/Co(1)–O(4)–V(1)	150.9(18)		

2.41 Å wavelength provided by the (113) reflection of a Germanium vertical focusing monochromator. Powder samples were loaded in aluminum cans inside a top loading Helium-3 cryostat capable of cooling to 0.3 K. The Mn-glaserite sample was also measured under several magnetic fields up to 4.5 T at 0.3 K. For these measurements the sample was pelletized to prevent rotation of the powder grains in the applied magnetic field. The field was directed perpendicular to the scattering plane. Additional diffraction measurements were performed using the POWGEN instrument at the Spallation Neutron Source (SNS). For those measurements, powder samples were loaded into 8 mm diameter vanadium holders and cooled down to 10 K by using a closed-cycle refrigerator. A temperature dependence study was carried out by collecting data continuously using the center neutron wavelengths of 1.333 Å while cooling the sample between 300 and 10 K at a nominal rate of 1.5 K/min. The data were rebinned into data sets every 8 K with a nominal counting time of about 14 min using the MANTID software. The neutron diffraction data were analyzed by using the FullProf Suite Package.³⁰

3. RESULTS AND DISCUSSION

3.1. Room-Temperature Crystal Structure. At room temperature, all three compounds Na₂BaM(VO₄)₂ (M = Mn, Mn_{0.6}Co_{0.4}, and Co) crystallize in a trigonal crystal system with space group of $\bar{P}3m1$. The detailed crystallographic information is given in Table 1. The unit cell parameters are as follows: for Na₂BaMn(VO₄)₂, $a = 5.5929(2)$ Å, $c = 7.1540(4)$ Å, and $V = 193.80(2)$ Å³, for Na₂BaCo(VO₄)₂, $a = 5.5440(2)$ Å, $c = 7.0668(4)$ Å, $V = 188.105(17)$ Å³, and, for Na₂BaMn_{0.6}Co_{0.4}(VO₄)₂, $a = 5.5761(2)$ Å, $c = 7.1245(5)$ Å, $V = 191.843(19)$ Å³. The crystal structure is built from 2D transition metal vanadate layers where Na⁺ and Ba²⁺ ion reside in between the layers, Figure 1a. The transition metal vanadate layers (M–O–V) are constructed from corner sharing MO₆-octahedra and VO₄-tetrahedra units along the *ab*-plane. In the trigonal structure, the M²⁺ ion is coordinated by six equivalent oxygen atoms, O(2), forming symmetrical MO₆-octahedra (MO₆-oct). The V⁵⁺ ion adopts a nearly symmetrical VO₄-tet from three O(2) atoms and one O(1) atom. As shown in Figure 1b, each MO₆-oct is surrounded by six VO₄-tet groups to form the M–O–V 2D lattice. The VO₄-tet groups connect with MO₆ units in up and down fashion where Na⁺ ions reside between the spaces. In Na₂BaMn(VO₄)₂, the Mn(1)–O(2) bond distance is 2.118(11) Å, and O(2)–Mn(1)–O(2) bond angles are 85.1(4) and 94.9(4)°, respectively. For Na₂BaCo-

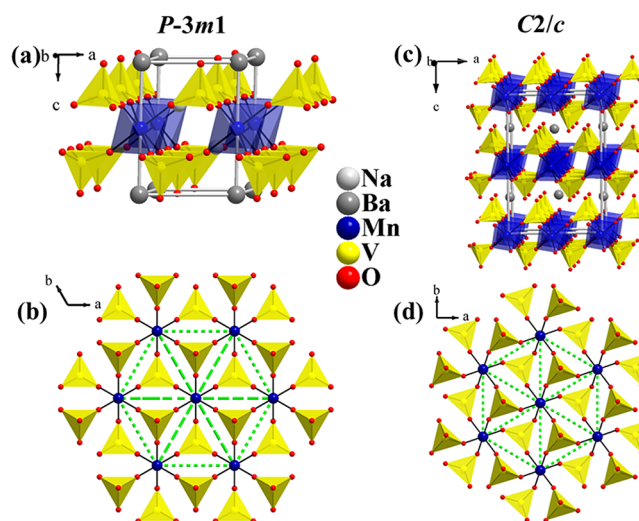


Figure 1. Crystal structures of trigonal, $\bar{P}3m1$ Na₂BaMn(VO₄)₂ (a) and monoclinic, C2/c Na₂BaMn(VO₄)₂ (c). Figure (b) and (d) display the connectivity between MnO₆ octahedra and VO₄ tetrahedra within the 2D lattice along the *ab*-plane for trigonal and monoclinic structures, respectively. The green dashed lines indicate the triangular magnetic lattice. The magnetic exchange happen via nonmagnetic VO₄ groups.

(VO₄)₂, the Co(1)–O(2) bond distance is 2.065(6) Å, and O(2)–Co(1)–O(2) bond angles are 85.7(2)° and 94.3(3)°. For Na₂BaMn_{0.6}Co_{0.4}(VO₄)₂, the Mn/Co(1)–O(2) bond distance is 2.099(7) Å, and O(2)–Mn/Co(1)–O(2) bond angles are 85.1(3) and 94.9(3)°. The V–O bond distance and O–V–O bond angles range from 1.679(8) to 1.685(7) Å and 108.4(2) to 110.5(2)° across the family of compounds. The interatomic distances and bond angles suggest that MO₆-oct and VO₄-tet belong to D_{3d} and C_{3v} symmetry groups and form a perfect triangular lattice where MO₆ units construct equilateral triangles as displayed in Figure 1b. The interatomic distances between M²⁺ ions within the triangle are 5.5929(2), 5.5440(2), and 5.5761(2) Å for Na₂BaMn(VO₄)₂, Na₂BaCo(VO₄)₂, and Na₂BaMn_{0.6}Co_{0.4}(VO₄)₂, respectively.

3.2. Phase Transition at Lower Temperature. At lower temperatures, both Na₂BaMn(VO₄)₂ and Na₂BaMn_{0.6}Co_{0.4}(VO₄)₂ compounds undergo a structural

transition from the trigonal space group $P\bar{3}m1$ to the monoclinic space group $C2/c$, which is similar to our previously reported compound $\text{Na}_2\text{BaFe}(\text{VO}_4)_2$.²⁷ The structural transition takes place at approximately 247 K for $\text{Na}_2\text{BaMn}(\text{VO}_4)_2$ and at about 186 K for the intermediate compound $\text{Na}_2\text{BaMn}_{0.6}\text{Co}_{0.4}(\text{VO}_4)_2$, compared to around 290 K for $\text{Na}_2\text{BaFe}(\text{VO}_4)_2$.²⁷ The structural transition has been confirmed by both single crystal and powder diffraction studies. Systematic temperature dependence measurements performed using neutron powder diffraction of $\text{Na}_2\text{BaMn}(\text{VO}_4)_2$ and X-ray diffraction of $\text{Na}_2\text{BaMn}_{0.6}\text{Co}_{0.4}(\text{VO}_4)_2$ are summarized by the contour plots shown in Figure 2. The plots

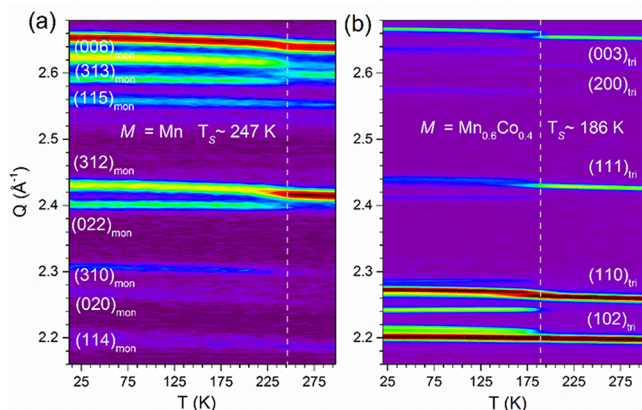


Figure 2. Contour plots showing the evolution of diffraction intensities across the structural transition that occurs in (a) $\text{Na}_2\text{BaMn}(\text{VO}_4)_2$ measured using neutron radiation and in (b) $\text{Na}_2\text{BaMn}_{0.6}\text{Co}_{0.4}(\text{VO}_4)_2$ measured using X-ray.

clearly display the splitting of trigonal reflections into multiple peaks below the structural transition. The large difference in peak intensities shown in Figure 2a,b is not entirely due to the difference in composition but to the large contrast in the relative scattering lengths and cross sections offered by the neutron and X-ray methods. In contrast to the Mn and mixed (Mn,Co) congeners, $\text{Na}_2\text{BaCo}(\text{VO}_4)_2$ did not show any

structural transition within the measured temperature range ($T \geq 300$ mK). The single crystal structure refinements suggest a slight degradation of crystal quality and/or twin formation while cooling through the phase transition.

We examined the lower symmetry structures in detail and compared them to the room-temperature structures. The lower symmetry monoclinic $C2/c$ space group allows two additional oxygen atomic positions compared to the higher symmetry structure (Table SI 1) which breaks the local symmetry of $\text{MO}_6\text{-oct}$ and $\text{VO}_4\text{-tet}$ to C_i and C_1 , respectively. The bond distances and angles for the lower symmetry ($C2/c$) structures are summarized in Table 3. The MnO_6 units in $C2/c$ - $\text{Na}_2\text{BaMn}(\text{VO}_4)_2$ possess a distorted octahedral geometry with four shorter equatorial Mn–O bonds and two longer apical Mn–O bonds. The Mn–O and V–O bond distances range from 2.134(10) to 2.176(10) Å and 1.683(9) to 1.732(10) Å, respectively. The average Mn–O and V–O bond distances are 2.157(10) and 1.712(10) Å in contrast to the $P\bar{3}m1$ structure, where the average Mn–O and V–O lengths are 2.117(10) and 1.682(10) Å. The deviation of average Mn–O and V–O bond distances (Δ) between trigonal and monoclinic structures are 0.02 and 0.03 Å, respectively. Bond angles of O–Mn–O and O–V–O vary from 83.8(4) to 96.2(4)° and from 107.6(5) to 111.2(5)°, respectively. It is worth mentioning the deviation of O–Mn–O and O–V–O bond angles in the monoclinic structure as compared to the original trigonal structure. In the monoclinic structure, two O(2)–Mn(1)–O(3) bond angles are 88.1(4) and 91.9(4)°, and two O(2)–Mn(1)–O(4) bond angles are 83.8(4) and 96.2(4)° compared to the O–Mn–O bond angles of 85.1(4)° and 94.9(4)° in trigonal structure. As a result of this deviation, both $\text{MnO}_6\text{-oct}$ and $\text{VO}_4\text{-tet}$ have to tilt along the *ab*-plane to connect in order to form the 2D Mn–O–V layered structure (Figure 1b). Therefore, Mn^{2+} ions in the $C2/c$ structure form isosceles triangles (Figure 3a) with Mn^{2+} – Mn^{2+} distances of 5.6285(4) and 5.5617(3) Å. Similar structural distortion can be observed in the mixed Mn/Co phase as well with shorter (Mn/Co)²⁺–(Mn/Co)²⁺ distances of 5.5480(4) and 5.5628(5) Å (Figure 3c). It is this distortion that is the manifestation of the phase change to lower

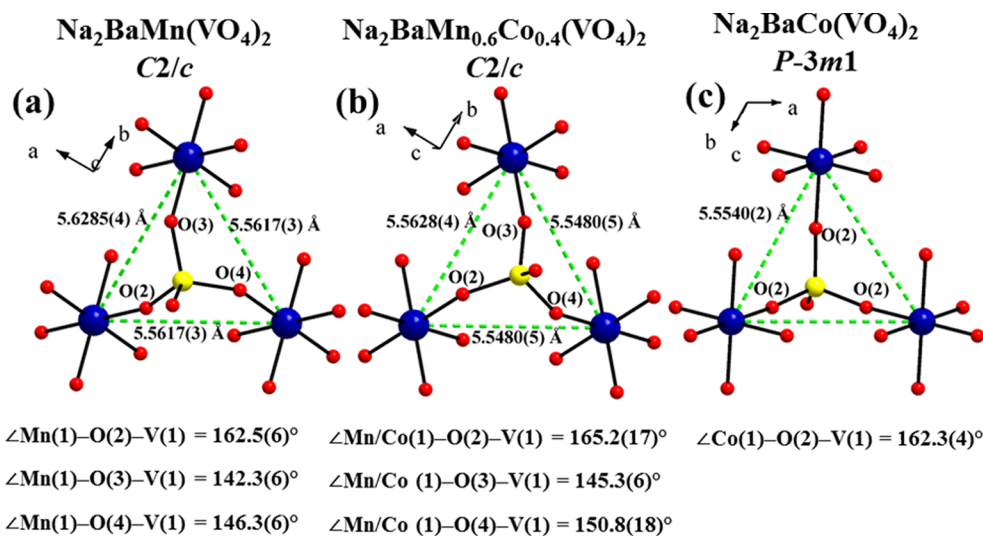


Figure 3. Comparison of the M^{2+} triangular unit of $\text{Na}_2\text{BaM}(\text{VO}_4)_2$ ($\text{M} = \text{Mn}, \text{Mn/Co}, \text{Co}$) series. $\text{Na}_2\text{BaM}(\text{VO}_4)_2$ ($\text{M} = \text{Mn}, \text{Mn/Co}$) structures are reported after the structural transition. The M–O–V bond angles are summarized, and $\text{Na}_2\text{BaM}(\text{VO}_4)_2$ ($\text{M} = \text{Mn}, \text{Mn/Co}$) show a tilting in M–O–V bond angles compare to M–O–V bond angles in $\text{Na}_2\text{BaCo}(\text{VO}_4)_2$ which break the 3-fold symmetry M^{2+} triangle along the *c*-axis.

symmetry and has a significant effect on the resultant magnetic behavior.

3.3. Magnetization and Heat Capacity Measurements. Results of magnetization measurements on the Mn-, Co-, and Co/Mn-glaserite phases are summarized in Figures 4

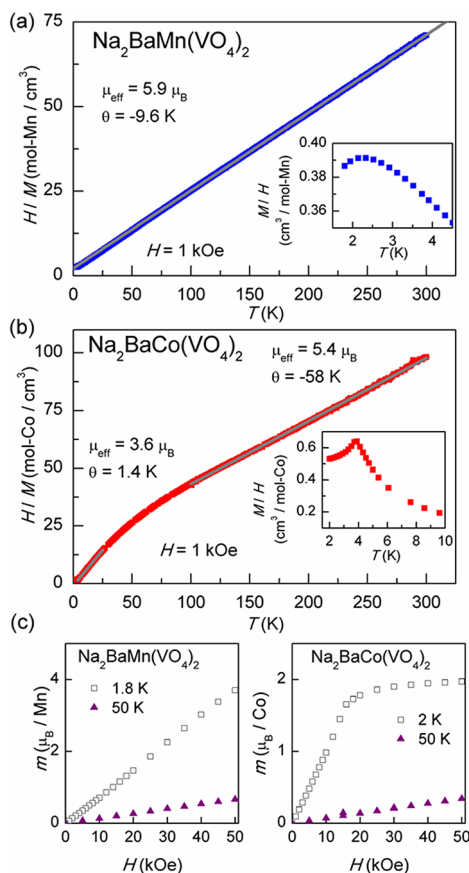


Figure 4. Results of magnetization measurements on $\text{Na}_2\text{BaMn}(\text{VO}_4)_2$ and $\text{Na}_2\text{BaCo}(\text{VO}_4)_2$ crystals collected with the applied field in the ab -plane. Inverse magnetic susceptibility (H/M) measured at 1 kOe; linear Curie–Weiss fits are shown in (a) and (b). The low-temperature behaviors of M/H are shown in the insets. Isothermal magnetization curves for the crystals are shown in (c).

and 5. Data are shown for the Mn- and Co-phases measured with the magnetic field in the ab -plane (Figure 4), and the results are in good agreement with those reported by Nakayama and co-workers.²⁸ A detailed discussion of the magnetic properties of these compounds can be found in ref 28, so the behavior will only be briefly described here. High-temperature Curie–Weiss fits give an effective moment $m_{\text{eff}} = 5.9(1) \mu_{\text{B}}$, as expected for divalent Mn in $\text{Na}_2\text{BaMn}(\text{VO}_4)_2$ ($S = 5/2$), but an effective moment of $m_{\text{eff}} = 5.4(1) \mu_{\text{B}}$ significantly larger than the spin only value for Co^{2+} in $\text{Na}_2\text{BaCo}(\text{VO}_4)_2$ ($S = 3/2$, $mS_{\text{eff}} = 3.8 \mu_{\text{B}}$). This is attributed an orbital component, which is not expected to be quenched in octahedral high spin Co^{2+} with one hole in the t_{2g} set. As described in ref 28, the deviation from this high temperature Curie–Weiss behavior in the Co compound indicates a crossover to a doublet ground state associated with the trigonally distorted octahedral coordination. The Curie–Weiss analysis was also performed between 5 and 25 K for Co-compound, and the resulting Curie–Weiss fits give an effective moment $m_{\text{eff}} = 3.6(1) \mu_{\text{B}}$ which is comparable to the spin-only

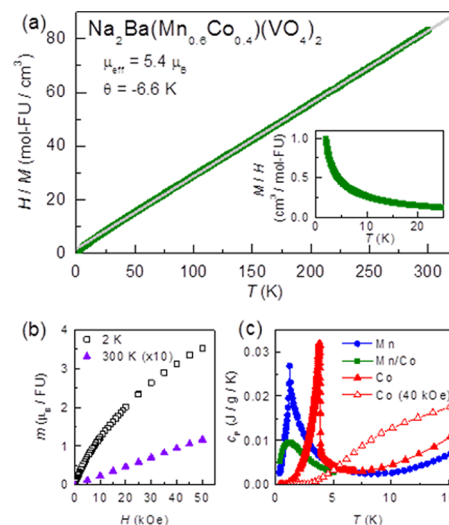


Figure 5. (a) Inverse magnetic susceptibility (H/M) and Curie–Weiss fit for a $\text{Na}_2\text{Ba}(\text{Mn}_{0.6}\text{Co}_{0.4})(\text{VO}_4)_2$ single crystal with low-temperature H/M data shown in the inset. (b) Isothermal magnetization curves at 2 and 300 K. (c) Low-temperature heat capacity of the three glaserite compounds measured in zero magnetic field and for the Co phase in a 40 kOe applied magnetic field.

value for Co^{2+} in $\text{Na}_2\text{BaCo}(\text{VO}_4)_2$ ($S = 3/2$, $mS_{\text{eff}} = 3.8 \mu_{\text{B}}$). However, one may also consider that the change in effective magnetic moment indicates a spin-state transition of the Co^{2+} ions from high-spin ($S = 3/2$) to low-spin ($S = 1/2$). The spin state transition may cause the gyromagnetic ratio, g , value to deviate largely from 2 as previously observed in many Co-based triangular magnetic lattices such as $\text{A}_4\text{CoB}_2\text{O}_{12}$ ($\text{A} = \text{Ba}, \text{Sr}, \text{La}$ and $\text{B} = \text{W}, \text{Re}$) series reported by Rawl et al.³¹ For $\text{Na}_2\text{BaCo}(\text{VO}_4)_2$, the calculated g value is 4.1 based on the spin 1/2 model for octahedrally coordinated Co^{2+} which is comparable with the previous report.²⁸ Furthermore, in that work, the effective moment was found to be anisotropic at low temperature, and a saturation moment close to 3 and $2 \mu_{\text{B}}/\text{Co}$ was observed at 2 K for H along the c -axis and in the ab -plane, respectively. This is consistent with the ab -plane data shown in Figure 4c. The low-temperature M/H behaviors shown in the insets of Figure 4a,b indicate a broad maximum near 2.5 K in $\text{Na}_2\text{BaMn}(\text{VO}_4)_2$, while $\text{Na}_2\text{BaCo}(\text{VO}_4)_2$ displays a sharper magnetic transition at about 4 K. The isothermal magnetization curve measured at 1.8 K is linear up to 50 kOe for the Mn-compound (Figure 4c), but saturation has been observed in higher fields and at lower temperatures.²⁸

Magnetic data from a $\text{Na}_2\text{Ba}(\text{Mn}_{0.6}\text{Co}_{0.4})(\text{VO}_4)_2$ single crystal is shown in Figure 5. These crystals did not grow with a platelike morphology, so the orientation of the crystal with respect to the field during the measurement is not known. The data shows Curie–Weiss behavior over a wide temperature range, with an effective moment $m_{\text{eff}} = 5.4(1) \mu_{\text{B}}$ that is close to the spin-only value of the mixture ($\text{Mn}^{2+}_{0.6}\text{Co}^{2+}_{0.4}$) ($m_{\text{eff}} = 5.1(1) \mu_{\text{B}}$). The small negative Weiss temperature of -6.6 K suggests the net interactions are weakly antiferromagnetic interactions. No clear indication of long-range magnetic ordering is seen down to 2 K, although there is an apparent upturn below about 5 K (Figure 5, inset). This suggests that the Mn–Co disorder suppresses the magnetic ordering in the glaserite structure.

Heat capacity measurements down to about 0.4 K were performed to look for signs of magnetic phase transitions at

lower temperature. The results are shown in Figure 5c. Similar data for $\text{Na}_2\text{BaMn}(\text{VO}_4)_2$ were reported in ref 28; a sharp cusp is seen at the magnetic ordering temperature of 1.3 K. The shape is not that of a typical lambda anomaly, but is skewed to higher temperatures. This may indicate the onset of some magnetic correlations before the long-range order sets in upon cooling. This is consistent with the magnetization data (Figure 4a), which begins to roll over upon cooling starting near 3–4 K, and the appearance of diffuse neutron scattering at low angles noted below. The heat capacity of the Co-glaserite phase shows a sharp lambda anomaly with a peak at 3.8 K, in agreement with the magnetization data (Figure 4b). This compound was also measured in a 40 kOe applied magnetic field, and it is seen that the thermal anomaly is shifted strongly to higher temperatures and broadened, which is behavior expected for a ferromagnetic transition. The mixed Mn/Co glaserite does not show any sharp features down to 0.40 K, and only a broad maximum centered near 1.2 K is observed. This may indicate the development of short-range magnetic order or freezing into a spin-glass-like state, either of which may be expected in this chemically disordered phase with competing ferromagnetic and antiferromagnetic interactions. Additional magnetic measurements below the 2 K would be needed to identify the magnetic ground state with further certainty.

3.4. Magnetic Structures from Neutron Diffraction. As previously discussed, the neutron diffraction data confirmed the structural transition occurring in the Mn-based compound at about 247 K. Upon cooling below 3 K, additional diffuse scattering appears at low angles, revealing the formation of short-range magnetic correlations. At approximately 1 K, well-defined magnetic peaks are observed that could be indexed using the monoclinic chemical unit cell and the propagation vector $\mathbf{k} = (1, 0, 0)$. The diffuse magnetic scattering seems to coexist with long-range magnetic order and persists down to the lowest measured temperature, 0.3 K. The evolution of the magnetic scattering with the temperature is shown in Figure 6a. An estimation of the correlation length can only be attempted for $T = 1.5$ K data, where only diffuse magnetic scattering is present. The diffuse magnetic scattering is

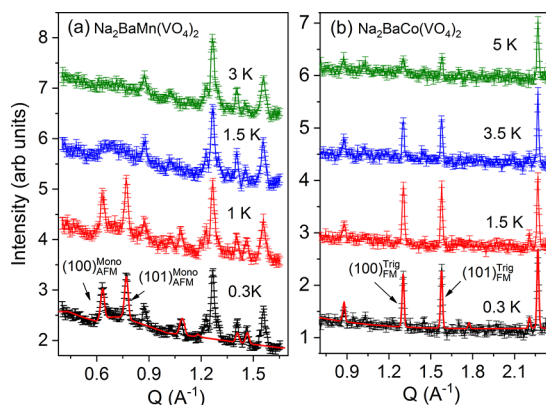


Figure 6. Low Q ($= 4\pi \sin \Theta/\lambda$) interval of the neutron diffracton patterns recorded at various temperatures for (a) $\text{Na}_2\text{BaMn}(\text{VO}_4)_2$ and (b) $\text{Na}_2\text{BaCo}(\text{VO}_4)_2$. Data reveals the presence of AFM magnetic Bragg peaks for Mn-based compound and FM orders for the Co variant. The solid lines drawn on top of the base temperature data represents the calculated profiles of magnetic scattering (for Mn) and magnetic and nuclear contributions (for Co) based on the models described in the text and presented in Figure 7.

obtained by subtracting the paramagnetic contribution measured at 12 K data from 1.5 K data and applying a correction for the Mn magnetic form factor decay with the momentum transfer Q . The correlation length (ξ) was obtained by fitting the Q dependence of the intensity to a Lorentzian line-shape $I(Q) = I_0 + (2A/\pi) \cdot w/[4(Q - Q_0)^2 - w^2]$, where $\xi = 2/w$. The fit yields a value $\xi = 7.7(5)$ Å, which corresponds to approximately one unit cell. The difference 1.5–12 K data and the Lorentzian fit are shown in the Figure SI 3.

Magnetic structure models were generated using the MAXMAGN program, available at the Bilbao crystallographic server.³² The best description of the magnetic peak intensities was obtained using an antiferromagnetic order described by the magnetic space group P_21/c (#14.84).³² The fit of the magnetic scattering present at 0.3 K is represented by solid red line in the Figure 6a. When fitting the magnetic Bragg peaks the diffuse scattering was considered as background and it was modeled by linear interpolation of selected points in the pattern. The magnetic structure consists of stacking anti-ferromagnetic planes along the c -axis. Within each plane the moments are ordered in a Néel-type arrangement and are pointing along the C_4 axis of the octahedra. There are two Mn layers in the magnetic unit cell with spins on one plane rotated by about 140 degrees around the c -axis with respect to the other, following the relative rotation of MnO_6 octahedra. The positions of the Mn moments and their relative orientation is as follows: $(0, 1/2, 0 | m_a, m_b, m_c)$, $(0, 1/2, 1/2 | m_a, m_b, m_c)$, $(1/2, 0, 0 | -m_a, -m_b, -m_c)$, $(1/2, 0, 1/2 | -m_a, m_b, -m_c)$. A graphical representation of the magnetic structure is shown in Figure 7a. The refined values of magnetic moment

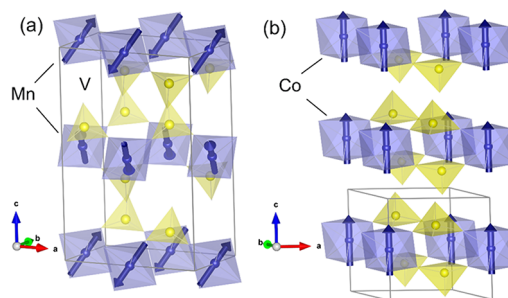


Figure 7. Antiferromagnetic structure of monoclinic $\text{Na}_2\text{BaMn}(\text{VO}_4)_2$ phase (a) and ferromagnetic order of trigonal $\text{Na}_2\text{BaCo}(\text{VO}_4)_2$ (b).

components at 0.3 K are $m_a = 0.5(2)\mu_B$, $m_b = 1.4(1)\mu_B$, $m_c = 1.4(1)\mu_B$, yielding a total ordered moment of $2.1(1)\mu_B$. This represents a significant reduction in magnitude compared to the expected value $g \cdot S = 5 \mu_B$ of Mn^{2+} , which is reasonable considering that appreciable short-range diffuse magnetic scattering coexists with the magnetic Bragg scattering.

As illustrated in Figure 8, on applying a magnetic field at 0.3 K the antiferromagnetic peaks (e.g., (100) and (101)) slowly drop in intensity with increasing field, and are nearly fully suppressed at about 4 T. Similar behavior is observed for the low- Q diffuse scattering magnetic. As this occurs, new magnetic scattering builds up at nuclear peak positions such as $(0, 0, 2)$, $(1, 1, 0)$, and $(1, 1, 2)$, suggesting an evolution toward a ferromagnetic-like state. The magnetic intensities are not saturated at our highest measured magnetic field of 4.5 T. Refinement of the magnetic moment at $\mu H = 4.5$ T indicate a magnetic moment of about $4.1(1)\mu_B$, that keeps the

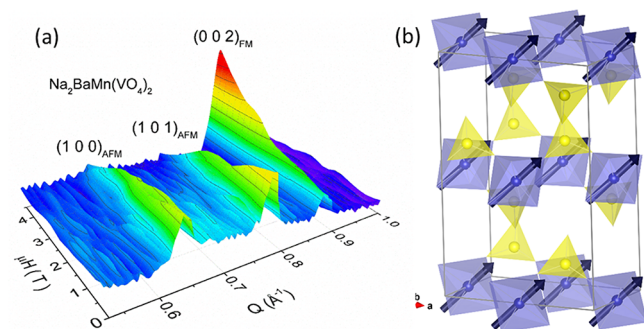


Figure 8. (a) Color surface map of the evolution of magnetic scattering of $\text{Na}_2\text{BaMn}(\text{VO}_4)_2$ in applied magnetic field. (b) Ferromagnetic structure of $\text{Na}_2\text{BaMn}(\text{VO}_4)_2$ at 4 T.

orientation nearly parallel to the C_4 axis of MnO_6 octahedra (see Figure 8b). The determined value of the ordered moment must be regarded with caution since the experiments were performed on random polycrystalline sample where the relative field direction with respect to the easy axis is neither unique nor well-defined.

In contrast with the Mn-compound, the $\text{Na}_2\text{BaCo}(\text{VO}_4)_2$ maintains its trigonal crystallographic structure down to the lowest measured temperatures, and the magnetic scattering that appears below approximately 4 K only contributes to the nuclear peak intensities ($\mathbf{k} = (0, 0, 0)$). No magnetic diffuse scattering is observed for this compound. The diffraction data is well-described by a ferromagnetic (FM) magnetic structure with Co moments aligned parallel to the c -axis direction. The magnetic space group of this FM order is $P\bar{3}m'1$ (#164.89).³² Data refinement reveals an ordered magnetic moment of $2.2(1) \mu_B$. This is lower than the expected spin-only moment of Co^{2+} ($3 \mu_B$). The calculated peak profiles consisting of magnetic and nuclear contributions is depicted by solid red line on top of 0.3 K data in Figure 6b. The pure magnetic contribution to the scattering obtained from subtracting 5 K data from 0.3 K is presented in the Supporting Information. The graphical representation of Co-based glaserite spin structure is displayed in Figure 7b.

4. SUMMARY

We have examined the structural and magnetic properties of two end members in the glaserite structure series, $\text{Na}_2\text{BaM}(\text{VO}_4)_2$ ($M = \text{Mn}$ and Co), as well as the intermediate composition $\text{Na}_2\text{BaMn}_{0.6}\text{Co}_{0.4}(\text{VO}_4)_2$. The pentavalent vanadium in the bridging groups has no d electrons, and the MO_6 octahedra interconnect through these nonmagnetic VO_4^{3-} groups. In addition, the Ba^{2+} cations separate two $M\text{--O--V}$ layers along the c -axis and weaken the interlayer magnetic interactions. The magnetization of our $\text{Na}_2\text{BaMn}(\text{VO}_4)_2$ and $\text{Na}_2\text{BaCo}(\text{VO}_4)_2$ reveals the presence of AFM and FM long-range ordering at low temperatures, respectively, which is similar to the report of Nakayama et al.²⁸ This is further confirmed by neutron powder diffraction. The mixed compound $\text{Na}_2\text{BaMn}_{0.6}\text{Co}_{0.4}(\text{VO}_4)_2$ does not show any long-range ordering down to 0.4 K, which is likely related to the mixed Mn/Co site occupancy and competing AFM/FM interactions.

The intralayer magnetic superexchange interactions take place via nonmagnetic vanadate bridging groups, $M^{2+}\text{--O}^{2-}\text{--V}^{5+}\text{--O}^{2-}\text{--M}^{2+}$. Therefore, it is important to discuss the change of $M\text{--O--V}$ bond angles between the structures in this series

of compounds and relate to their magnetic properties. Several noticeable structural features of Mn, Fe, and Co compounds are as follows: (i) Both $\text{Na}_2\text{BaMn}(\text{VO}_4)_2$ and $\text{Na}_2\text{BaFe}(\text{VO}_4)_2$ show crystallographic phase transitions below room temperatures. (ii) At room temperature, Mn, Fe, and Co trigonal structures have very similar $M\text{--O--V}$ bond angles which are $161.8(6)$, $161.7(4)$, and $162.3(4)^\circ$. (iii) In low-temperature, monoclinic $\text{Na}_2\text{BaMn}(\text{VO}_4)_2$ and $\text{Na}_2\text{BaFe}(\text{VO}_4)_2$, the $M\text{--O--V}$ bond angles vary from $142.3(6)$ to $162.5(6)^\circ$ and from $142.7(4)$ to $164.1(4)^\circ$, respectively. Compared to Mn-derivatives, both $M\text{--O}(2)\text{--V}$ and $M\text{--O}(4)\text{--V}$ bond angles are slightly larger in $\text{Na}_2\text{BaFe}(\text{VO}_4)_2$. The $M\text{--O}(2)\text{--V}$ and $M\text{--O}(4)\text{--V}$ bond angles for Mn are $162.5(4)$ and $146.3(6)^\circ$, and those for Fe are $164.1(4)$ and $148.0(4)^\circ$. This small difference in the $M\text{--O--V}$ bond angles changes the relative orientation of the transition metal octahedra and vanadate tetrahedra which makes $\text{Na}_2\text{BaMn}(\text{VO}_4)_2$ and $\text{Na}_2\text{BaFe}(\text{VO}_4)_2$ antiferromagnetic and ferromagnetic at low temperatures, respectively.²⁷ The present study illustrates how strongly correlated the crystal structures are with magnetic ground state in the glaserite structure series. It would be interesting to examine if replacing Na^+ and Ba^{2+} cations in the structure could preserve 3-fold symmetry at lower temperatures, which could suppress the structural transition and presumably maintain the triangular antiferromagnetic lattice with multiferroicity.

■ ASSOCIATED CONTENT

Supporting Information

The Supporting Information is available free of charge on the ACS Publications website at DOI: [10.1021/acs.inorgchem.8b03418](https://doi.org/10.1021/acs.inorgchem.8b03418).

Positional parameters, table of elemental analysis, powder X-ray diffraction figures, magnetic scattering figures (PDF)

Accession Codes

CCDC 1859758–1859763 contain the supplementary crystallographic data for this paper. These data can be obtained free of charge via www.ccdc.cam.ac.uk/data_request/cif, or by emailing data_request@ccdc.cam.ac.uk, or by contacting The Cambridge Crystallographic Data Centre, 12 Union Road, Cambridge CB2 1EZ, UK; fax: +44 1223 336033.

■ AUTHOR INFORMATION

Corresponding Author

*E-mail: kjoseph@clemson.edu.

ORCID

Michael A. McGuire: 0000-0003-1762-9406

Colin D. McMillen: 0000-0002-7773-8797

Notes

The authors declare no competing financial interest.

■ ACKNOWLEDGMENTS

The authors thank the National Science Foundation Grant No. DMR-1410727 for financial support. Work at the Oak Ridge National Laboratory, was sponsored by the Scientific User Facilities Division (neutron diffraction) and Materials Sciences and Engineering Division (magnetization measurements), Office of Basic Energy Sciences, U.S. Department of Energy (DOE).

REFERENCES

- (1) Lacroix, C.; Mendels, P.; Mila, F. *Introduction to Frustrated Magnetism: Materials, Experiments, Theory*; Springer Series in Solid State Sciences; Berlin: Springer, 2011.
- (2) Coldea, R.; Tennant, D. A.; Tsvetlik, A. M.; Tyliczynski, Z. Experimental Realization of a 2D Fractional Quantum Spin Liquid. *Phys. Rev. Lett.* **2001**, *86*, 1335.
- (3) Shores, M. P.; Nytko, E. A.; Bartlett, B. M.; Nocera, D. G. A Structurally Perfect $S = 1/2$ Kagome Antiferromagnet. *J. Am. Chem. Soc.* **2005**, *127*, 13462–13463.
- (4) Grohol, D.; Nocera, D. G.; Papoutsakis, D. Magnetism of Pure Jarosites. *Phys. Rev. B: Condens. Matter Mater. Phys.* **2003**, *67*, No. 064401.
- (5) Norman, M. R. Colloquium: Herbertsmithite and the Search for the Quantum Spin Liquid. *Rev. Mod. Phys.* **2016**, *88*, No. 041002.
- (6) Balents, L. Spin Liquids in Frustrated Magnets. *Nature* **2010**, *464*, 199–208.
- (7) Pratt, F. L.; Baker, P. J.; Blundell, S. J.; Lancaster, T.; Ohira-Kawamura, S.; Baines, C.; Shimizu, Y.; Kanoda, K.; Watanabe, I.; Saito, G. Magnetic and Non-magnetic Phases of a Quantum Spin Liquid. *Nature* **2011**, *471*, 612–616.
- (8) Dong, Z.-H.; Gu, S.-W. Magnetic Properties of the Triangular-lattice Multilayer Antiferromagnet with Single-site Anisotropy. *J. Phys.: Condens. Matter* **2000**, *12*, 2819.
- (9) Fortune, N. A.; Hannahs, S. T.; Yoshida, Y.; Sherline, T. E.; Ono, T.; Tanaka, H.; Takano, Y. Cascade of Magnetic-Field-Induced Quantum Phase Transitions in a Spin- $1/2$ Triangular-Lattice Antiferromagnet. *Phys. Rev. Lett.* **2009**, *102*, 257201.
- (10) Kodama, K.; Takigawa, M.; Horvatić, M.; Berthier, C.; Kageyama, H.; Ueda, Y.; Miyahara, S.; Becca, F.; Mila, F. Magnetic Superstructure in the Two-Dimensional Quantum Antiferromagnet $\text{SrCu}_2(\text{BO}_3)_2$. *Science* **2002**, *298*, 395–399.
- (11) Svistov, L. E.; Smirnov, A. I.; Prozorova, L. A.; Petrenko, O. A.; Demianets, L. N.; Shapiro, A. Y. Quasi-two-dimensional Antiferromagnet on a Triangular Lattice $\text{RbFe}(\text{MoO}_4)_2$. *Phys. Rev. B: Condens. Matter Mater. Phys.* **2003**, *67*, No. 094434.
- (12) Ishii, R.; Tanaka, S.; Onuma, K.; Nambu, Y.; Tokunaga, M.; Sakakibara, T.; Kawashima, N.; Maeno, Y.; Broholm, C.; Gautreaux, D. P.; et al. Successive Phase Transitions and Phase Diagrams for the Quasi-two-dimensional Easy-axis Triangular Antiferromagnet $\text{Rb}_4\text{Mn}(\text{MoO}_4)_3$. *EPL* **2011**, *94*, 17001.
- (13) Ono, T.; Tanaka, H.; Katori, H. A.; Ishikawa, F.; Mitamura, H.; Goto, T. Magnetization Plateau in the Frustrated Quantum Spin System Cs_2CuBr_4 . *Phys. Rev. B: Condens. Matter Mater. Phys.* **2003**, *67*, 104431.
- (14) Alicea, J.; Chubukov, A. Y.; Strykh, O. A. Quantum Stabilization of the $1/3$ -Magnetization Plateau in Cs_2CuBr_4 . *Phys. Rev. Lett.* **2009**, *102*, 137201.
- (15) Shirata, Y.; Tanaka, H.; Matsuo, A.; Kindo, K. Experimental Realization of a Spin- $1/2$ Triangular-Lattice Heisenberg Antiferromagnet. *Phys. Rev. Lett.* **2012**, *108*, No. 057205.
- (16) Susuki, T.; Kurita, N.; Tanaka, T.; Nojiri, H.; Matsuo, A.; Kindo, K.; Tanaka, H. Magnetization Process and Collective Excitations in the $S = 1/2$ Triangular-Lattice Heisenberg Antiferromagnet $\text{Ba}_3\text{CoSb}_2\text{O}_9$. *Phys. Rev. Lett.* **2013**, *110*, 267201.
- (17) Hwang, J.; Choi, E. S.; Ye, F.; Dela Cruz, C. R.; Xin, Y.; Zhou, H. D.; Schlottmann, P. Successive Magnetic Phase Transitions and Multiferroicity in the Spin-One Triangular-Lattice Antiferromagnet $\text{Ba}_3\text{NiNb}_2\text{O}_9$. *Phys. Rev. Lett.* **2012**, *109*, 257205.
- (18) Lee, M.; Choi, E. S.; Ma, J.; Sinclair, R.; Dela Cruz, C. R.; Zhou, H. D. Magnetism and Multiferroicity of an Isosceles Triangular Lattice Antiferromagnet $\text{Sr}_3\text{NiNb}_2\text{O}_9$. *J. Phys.: Condens. Matter* **2016**, *28*, 476004.
- (19) Lee, M.; Hwang, J.; Choi, E. S.; Ma, J.; Dela Cruz, C. R.; Zhu, M.; Ke, X.; Dun, Z. L.; Zhou, H. D. Series of Phase Transitions and Multiferroicity in the Quasi-two-dimensional Spin- $1/2$ Triangular-lattice Antiferromagnet $\text{Ba}_3\text{CoNb}_2\text{O}_9$. *Phys. Rev. B: Condens. Matter Mater. Phys.* **2014**, *89*, 104420.
- (20) Lee, M.; Choi, E. S.; Huang, X.; Ma, J.; Dela Cruz, C. R.; Matsuda, M.; Tian, W.; Dun, S. L.; Dong, S.; Zhou, H. D. Magnetic Phase Diagram and Multiferroicity of $\text{Ba}_3\text{MnNb}_2\text{O}_9$: A spin- $5/2$ Triangular Lattice Antiferromagnet with Weak Easy-axis Anisotropy. *Phys. Rev. B: Condens. Matter Mater. Phys.* **2014**, *90*, 224402.
- (21) Ribeiro, J. L.; Perez-Mato, J. Symmetry and Magnetic Field Driven Transitions in the 2D Triangular Lattice Compound $\text{RbFe}(\text{MoO}_4)_2$. *J. Phys.: Condens. Matter* **2011**, *23*, 446003.
- (22) Smolensky, G. A.; Prokhorova, S. D.; Siny, I. G.; Fousková, A.; Koňák, Č.; Dudnik, E. F. Phase Transitions in Ferroelastic $\text{KFe}(\text{MoO}_4)_2$. *Ferroelectrics* **1980**, *26*, 677–680.
- (23) Smirnov, A. I.; Svistov, L. E.; Prozorova, L. A.; Zheludev, A.; Lumsden, M. D.; Ressouche, E.; Petrenko, O. A.; Nishikawa, K.; Kimura, S.; Hagiwara, M.; Kindo, K.; Shapiro, A. Y.; Demianets, L. N. Chiral and Collinear Ordering in a Distorted Triangular Antiferromagnet. *Phys. Rev. Lett.* **2009**, *102*, No. 037202.
- (24) Amuneke, N. E.; Tapp, J.; de la Cruz, C. R.; Möller, A. Experimental Realization of a Unique Class of Compounds: XY-Antiferromagnetic Triangular Lattices, $\text{KAg}_2\text{Fe}[\text{VO}_4]_2$ and $\text{RbAg}_2\text{Fe}[\text{VO}_4]_2$, with Ferroelectric Ground States. *Chem. Mater.* **2014**, *26*, 5930–5935.
- (25) Möller, A.; Amuneke, N. E.; Daniel, P.; Lorenz, B.; de la Cruz, C. R.; Gooch, M.; Chu, P. C. $\text{A} \text{Ag}_2\text{M}[\text{VO}_4]_2$ ($\text{A} = \text{Ba}, \text{Sr}$; $\text{M} = \text{Co}, \text{Ni}$): A Series of Ferromagnetic Insulators. *Phys. Rev. B: Condens. Matter Mater. Phys.* **2012**, *85*, 214422.
- (26) Sanjeeva, L. D.; McMillen, C. D.; Willett, D.; Chumanov, G.; Kolis, J. W. Hydrothermal Synthesis of Single Crystals of Transition Metal Vanadates in the Glaserite Phase. *J. Solid State Chem.* **2016**, *236*, 61–68.
- (27) Sanjeeva, L. D.; Garlea, V. O.; McGuire, M. A.; Frontzek, M.; McMillen, C. D.; Fulle, K.; Kolis, J. W. Investigation of a Structural Phase Transition and Magnetic Structure of $\text{Na}_2\text{BaFe}(\text{VO}_4)_2$: A Triangular Magnetic Lattice with a Ferromagnetic Ground State. *Inorg. Chem.* **2017**, *56*, 14842–14849.
- (28) Nakayama, G.; Hara, S.; Sato, H.; Narumi, Y.; Nojiri, H. Synthesis and Magnetic Properties of a New Series of Triangular-lattice Magnets, $\text{Na}_2\text{BaMV}_2\text{O}_8$ ($\text{M} = \text{Ni}, \text{Co}$, and Mn). *J. Phys.: Condens. Matter* **2013**, *25*, 116003.
- (29) Sheldrick, G. M. A Short History of SHELX. *Acta Crystallogr., Sect. A: Found. Crystallogr.* **2008**, *64*, 112–122.
- (30) Rodríguez-Carvajal, J. Recent Developments of the Program FULLPROF, Commission on Powder Diffraction (IUCr). *Newsletter* **2001**, *26*, 12–19.
- (31) Rawl, R.; Lee, M.; Choi, E. S.; Li, G.; Chen, K. W.; Baumbach, R.; delacruz, C. R.; Ma, J.; Zhou, H. D. Magnetic Properties of the Triangular Lattice Magnets $\text{AB}'\text{B}_2\text{O}_{12}$ ($\text{A} = \text{Ba}, \text{Sr}, \text{La}$, $\text{B}' = \text{Co}, \text{Ni}, \text{Mn}$; $\text{B} = \text{W}, \text{Re}$). *Phys. Rev. B: Condens. Matter Mater. Phys.* **2017**, *95*, 174438.
- (32) Perez-Mato, J. M.; Gallego, S. V.; Tasci, E. S.; Elcoro, L.; de la Flor, G.; Aroyo, M. I. Symmetry-Based Computational Tools for Magnetic Crystallography. *Annu. Rev. Mater. Res.* **2015**, *45*, 217–248. Server is available at <http://www.cryst.ehu.es>.